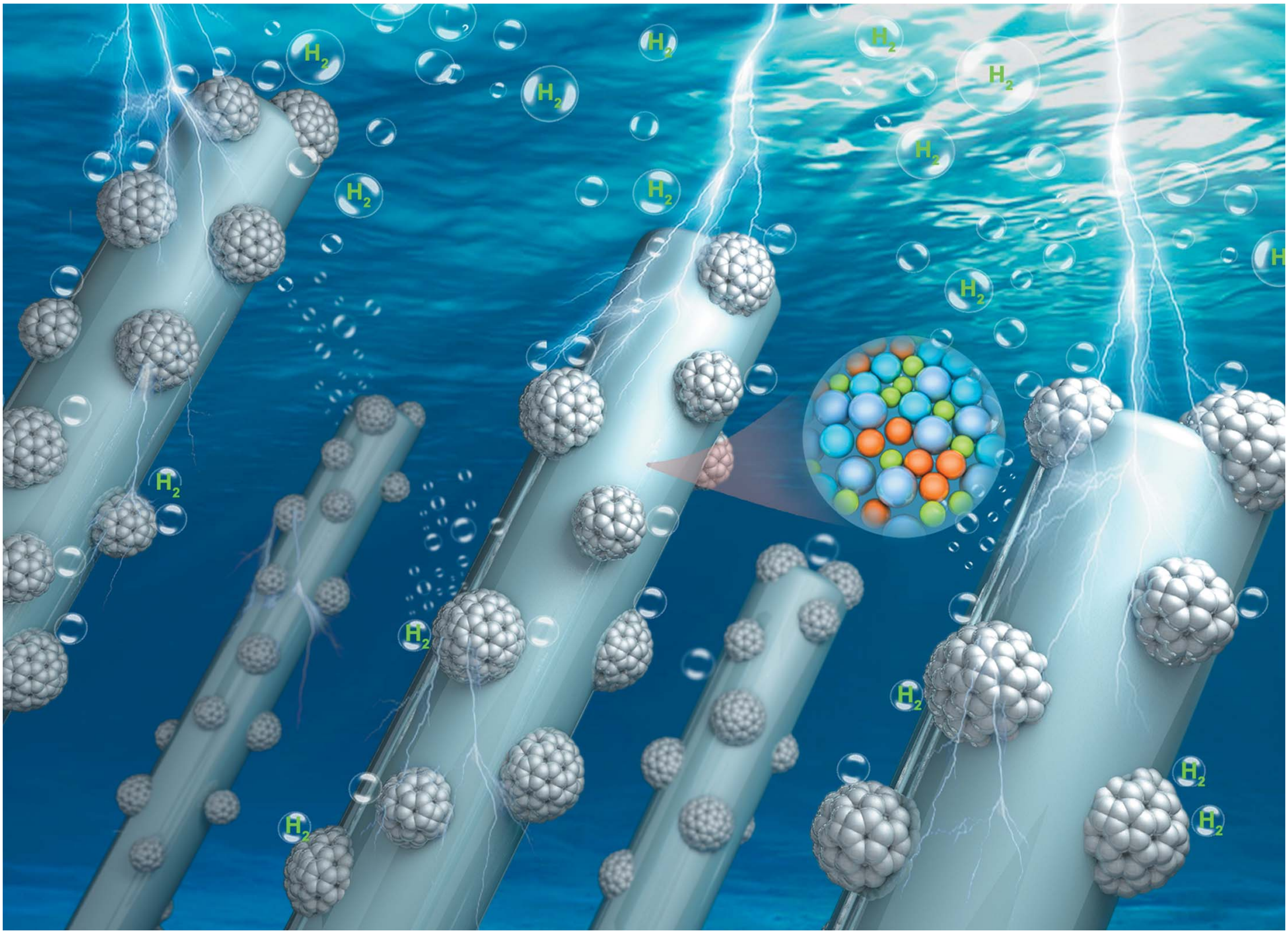

Highlighting a study by a group of researchers led by Prof. Jiang Ma from Shenzhen University.

Highly efficient and robust catalysts for the hydrogen evolution reaction by surface nano engineering of metallic glass

A flexible and universal strategy to synthesize hierarchical catalysts with excellent hydrogen evolution reaction performance was proposed by decorating Pt particles on a nanoengineered metallic glass surface. The Tafel slope is only 19.8 mV dec^{-1} and the catalyst is ultra-stable, showing enhanced catalytic performance at an overpotential of 200 mV for 500 hours.

As featured in:

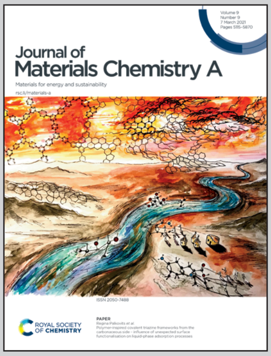

Volume 9
Number 9
7 March 2021
Pages 5115–5870

Journal of
Materials Chemistry A
Materials for energy and sustainability
rsc.li/materials-a

ISSN 2050-7488

ROYAL SOCIETY
OF CHEMISTRY

PAPER
Regina Palkovits *et al.*
Polymer-inspired covalent triazine frameworks from the carbonaceous side – influence of unexpected surface functionalisation on liquid-phase adsorption processes

See Jiang Ma *et al.*,
J. Mater. Chem. A, 2021, **9**, 5415.

ROYAL SOCIETY
OF **CHEMISTRY**

rsc.li/materials-a

Journal of
Materials Chemistry A

PAPER

Cite this: *J. Mater. Chem. A*, 2021, **9**, 5415

Highly efficient and robust catalysts for the hydrogen evolution reaction by surface nano engineering of metallic glass†

Yuqiang Yan,‡[ab] Chao Wang,‡[c] Zhiyuan Huang,[a] Jianan Fu,[a] Zezhou Lin,[a] Xi Zhang,[a] Jiang Ma*[a] and Jun Shen[a]

Received 20th October 2020
Accepted 18th December 2020

DOI: 10.1039/d0ta10235k

rsc.li/materials-a

Efficiency and stability are the key parameters for the hydrogen evolution reaction (HER) of water electrolysis, and therefore developing effective and robust catalysts has been a long standing pursuit. In this work, we propose a flexible and universal strategy to synthesize catalysts with excellent HER catalytic performance. Following this strategy, we successfully fabricate a hybrid electrocatalyst by decorating Pt particles on a nano engineered metallic glass (MG) surface (Pt@MG NWs). The overpotential of the catalyst to achieve a geometric current density of 10 mA cm^{-2} is 48.5 mV in 0.5 M H_2SO_4. Astonishingly, the Tafel slope is only 19.8 mV dec^{-1}, smaller than that of commercial 10% Pt/C. The Pt@MG NWs exhibit excellent charge transport efficiency and contain around 3 times more active sites than 10% Pt/C. In addition, the Pt@MG NWs are ultra-stable, exhibiting no degradation after the HER at overpotentials of 48.5 mV and 84 mV for 20 hours. Furthermore, this catalyst shows enhanced catalytic performance when a large working current is applied at an overpotential of 200 mV for 500 hours. The hydrophilicity and aerophobicity of Pt@MG NWs, which originate from surface structural construction, are responsible for the outstanding HER catalytic performance. The calculations found that the hybrid electrocatalyst exhibits small Gibbs free energy and strong H_2O adsorption energy. Our results provide a novel and universal approach for designing superior HER catalysts with excellent activity and stability.

Introduction

Hydrogen (H_2) is a promising energy carrier used as a fuel for both storage and transportation owing to its advantages (*e.g.*, high energy density, environmental friendliness, and natural abundance).[1,2] Among the current technologies for H_2 production, water electrolysis has attracted much attention due to its low cost and high energy conversion efficiency.[3–8] To accelerate the intrinsically slow kinetics of water electrolysis, developing highly active and long-term stable catalysts is now the most dominant strategy. To date, platinum (Pt)-based materials have been found to be the most efficient catalysts for the cathodic hydrogen evolution reaction (HER), but their commercialization has been severely hindered by the high cost and scarcity of Pt. To reduce the Pt dependence of HER catalysts, Pt-free catalysts have been widely synthesized, such as 3d transition metals,[9–11] molybdenum-based materials including MoS_2,[3,12–15] $MoSe_2$,[16–18] Mo_2C,[19,20] MoB,[20] MoS_2 analogues,[21] $NiMoN_x$,[22] and $Co_{0.6}Mo_{1.4}N_2$,[23] phosphates,[24,25] and chalcogenides.[26] Unfortunately, the durability of these catalysts is still not satisfactory when they are combined with strongly acidic electrolytes under long-term use, which cannot meet the requirements of large-scale industrial hydrogen production.

So far, Pt-based materials have remained the most efficient HER catalysts due not only to their high intrinsic electrocatalytic activity but also to their combinability with other materials to achieve superior catalytic performance. To develop low-cost Pt-based catalysts, two main strategies have been proposed to reduce the Pt loading while maintaining high catalytic activity. One strategy is to reduce the dimensions of Pt where more active sites are exposed on the surface. Pt nanoparticles supported on different supporters have been synthesis, *e.g.*, Pt@carbon,[27,28] Pt@TiO_2 (ref. 29 and 30) and Pt@metal boron organic polymers.[31] The dimensions of Pt have been further decreased down to a thin film, a monolayer, and even a single atom to increase catalytic activity.[32,33] The metal alloying process is another strategy where decoration of other transition metal species could promote catalytic activity *via* effectually downshifting the d-band center of Pt, *e.g.*, PtPd,[34] PtCu,[35] PtNi and PtNiCo.[36] By combining the above two strategies, many bimetallic and trimetallic Pt-based nanomaterials have been developed to reduce the use of precious metals

---

[a] *College of Mechatronics and Control Engineering, Shenzhen University, Shenzhen 518060, PR China. E-mail: majiang@szu.edu.cn*

[b] *Songshan Lake Materials Laboratory, Dongguan 523808, PR China*

[c] *Institute of Physics, Chinese Academy of Sciences, Beijing 100190, PR China*

† Electronic supplementary information (ESI) available. See DOI: 10.1039/d0ta10235k

‡ These authors contributed equally to this work.

without sacrificing efficiency. However, the poor conductivity of supporters and the large contact resistance between catalysts and supporters hinder their long-term application, especially under large current.

As a new class of amorphous material, metallic glass (MG) has gained a lot of attention since its discovery.[37–43] MG can be thermoplastically formed like plastics when heated or ultrasonic beating is applied, as its viscosity drops dramatically in the supercooled liquid region (SLR).[44] Benefiting from this property, various micro to nano structures can be fabricated on the MG surface. Meanwhile, owing to its amorphous nature, dealloying will occur when an electrochemical experiment is performed, which will expose more active sites on the surface.[45,46] Herein, through constructing dense nanowires (NWs) on the surface of a PdNiCuP MG by surface engineering, we designed a novel hybrid electrocatalyst consisting of Pt nanoparticles embedded in the MG matrix. The high conductivity of the composite structure and the high activity of Pt hybridized with Pd[47] led to a highly efficient and robust HER catalyst with superb performance at large current density and long-term stability.

Experimental

Preparation of the MG

The PdNiCuP bulk glassy alloy was chosen for the present study because this MG has been proven to have good flow properties and to be thermally stable in its SLR, which meet the requirements for thermoplastic forming (as shown in Fig. S1†). In addition, this composition has been demonstrated to be feasible for use as an HER electrocatalyst in its ribbon form.[45] A PdNiCuP MG rod with a diameter of 5 mm was prepared from a master alloy with a nominal composition of Pd 40 at%, Ni 10 at%, Cu 30 at%, and P 20 at% by the conventional water cooled copper mould casting method. For the convenience of thermoplastic forming, the rod was cut into disks with a thickness of ~1 mm and then polished using abrasive paper and a polishing machine.

Physical characterization

The amorphous nature of the as-cast MG and MG NWs was ascertained by X-ray diffraction (XRD; Rigaku MiniFlex600) with Cu Kα radiation and differential scanning calorimetry (DSC; PerkinElmer DSC-8000) at a heating rate of 20 K min^{-1}. Inductively coupled plasma-mass spectrometry (ICP-MS, Agilent 7700) was used to determine the loading mass of Pt on the catalysts. Surface chemical-state analysis was determined by using X-ray photoelectron spectroscopy (XPS, ThermoFisher ESCALAB Xi+). All binding energies were calibrated at the C 1s position (284.4 eV) of contaminant carbon in the vacuum chamber of the instrument.

The morphologies and elemental distributions of the samples were characterized using an FEI Quanta 450 FEG scanning electron microscope (SEM) instrument, a JEOL 2100F scanning transmission electron microscope (STEM) equipped with double spherical aberration (Cs) correctors and energy dispersive spectroscopy (EDS). The TEM samples were prepared on an FEI Scios scanning electron microscope/focused-ion beam (SEM/FIB) system.

Preparation of the Pt@MG NW catalysts

The Pt@MG NW catalysts were synthesized by using a CHI660E electrochemical workstation in a standard three-electrode system, using MG nanowires as the working electrode, a platinum wire as the counter electrode, and a saturated calomel electrode (SCE) as the reference electrode. First, the working electrode was cleaned by performing 50 cycles of cyclic voltammetry (CV) with a scan rate of 100 mV s^{-1} from 1.2 V to −0.2 V in 0.5 M H_2SO_4. Later, the Pt@MG NW catalysts were prepared by 1000 cycles of CV with a scan rate of 100 mV s^{-1} from 0.1 V to −0.2 V.[48,49] By using ICP-MS, the loading of Pt is measured to be 44.09 μg cm^{-2} (shown in Table S3†).

Electrochemical measurements

The electrocatalytic activities toward the HER were evaluated on an electrochemical workstation (CHI 660E, Chenhua, Shanghai, China) in a standard three-electrode mode with a PEM at room temperature. A platinum sheet was used as the counter electrode and a saturated calomel electrode (SCE) was used as the reference electrode. All the electrochemical measurements were performed in 0.5 M H_2SO_4. For comparison, the electrochemical performance of commercial 10 wt% Pt/C with a loading of 0.708 mg cm^{-2} was tested, which was prepared with 10 μL ink (Pt/C 5 mg mL^{-1}) and loaded onto a clean glassy carbon electrode (GCE, 3 mm in diameter). The HER activities were evaluated by linear sweep voltammetry (LSV) at 2 mV s^{-1}. The potential values reported in this study are *versus* the reversible hydrogen electrode (RHE) and are transformed to E *vs.* RHE using the equation $E(vs.\ \mathrm{RHE}) = E(\mathrm{SCE}) + 0.241\ \mathrm{V}$. Tafel plots were fitted to the Tafel equation: $\eta = b \log j + a$, where η is the overpotential, b is the Tafel slope, j is the current density, and a is the Tafel intercept relative to the exchange current density j_0. Cyclic voltammetry (CV) was carried out with various scan rates between 0.1 and 0.2 V *vs.* RHE to estimate the electrochemically active surface area (ECSA). Electrochemical impedance spectroscopy (EIS) was performed with frequencies ranging from 10^{-2} Hz to 10^{5} Hz with an amplitude of 5 mV. The durability measurements were carried out by using two methods: one was the chronoamperometry method at different static overpotentials, and the other was 10 000 cycles of LSV with a scan rate of 50 mV s^{-1} from 0.1 V to −0.2 V.

Results and discussion

Surface nano engineering to synthesise the hybrid electrocatalyst

Fig. 1a shows the basic principle of how the hybrid electrocatalyst Pt@MG NWs were fabricated. The polished MG plate was stacked with an anodic aluminum oxide (AAO) template that had nano-scale cavities (300 nm) on the surface. The MG plate was then heated up into its SLR in a custom-design vacuum furnace with a vacuum lever better than 10^{-3} Pa.

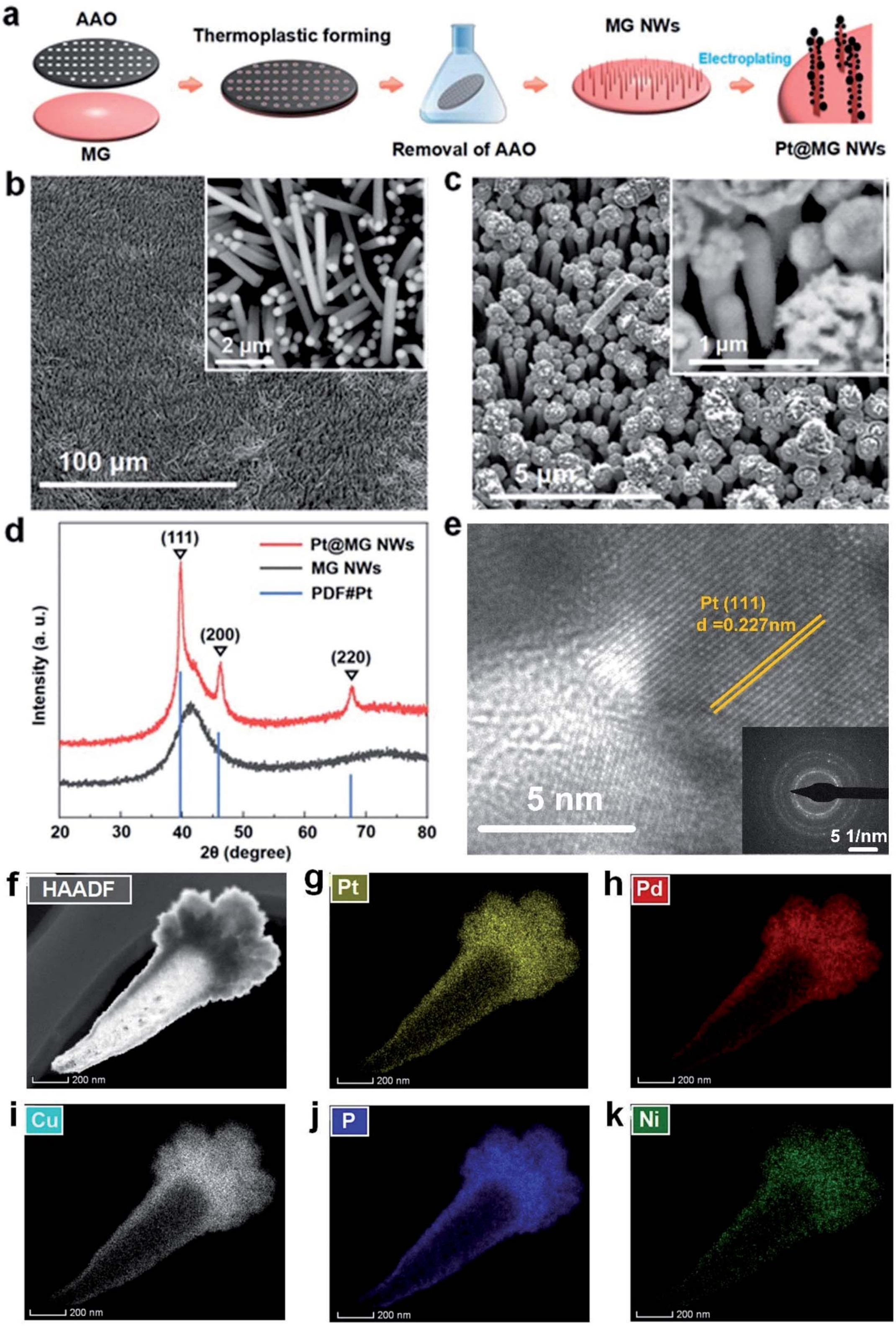

Fig. 1 Fabrication of the hybrid electrocatalyst for the HER. (a) Sketches for Pt@MG NW fabrication, including the thermoplastic forming, AAO removal and electroplating of fine Pt particle processes; (b) the SEM image of the MG surface with grass-like nanowires. The inset shows the magnified image of the nanowires; (c) the SEM image of Pt@MG NWs with the inset showing the magnified image; (d) the XRD patterns of Pt@MG NWs, MG and PDF#Pt; (e) HAADF image showing the atomic structure of Pt nanocrystals where fine Pt particles are decorated on the glassy nanowires; the inset shows the selected area electron diffraction pattern, illustrating Pt nanocrystals embedded in the MG matrix. (f–k) The element distribution of the as-fabricated Pt@MG NWs.

After the viscous MG filled the AAO template under a pressure of 200 MPa, a MG surface with NWs was obtained after removal of the AAO template in NaOH solution. The glassy nature was confirmed by using a TEM (shown in Fig. S2†). Then the MG NWs were placed in H_2SO_4 solution as substrates for Pt deposition. With a Pt wire as the anode, the Pt ions in the solution moved to the MG NWs to obtain electrons, and an ultrathin layer of Pt nanocrystals was plated on the surface of MG NWs; the details are stated in the ESI.† Fig. 1b shows the morphology of MG NWs, where grass-like nanowires with an average diameter of 300 nm are densely distributed over a large area. The inset in Fig. 1b exhibits the magnified image of the nanowires. As shown in Fig. 1c and the inset, the specific surface area of the Pd-NWs became larger after deposition of fine Pt particles, which presented a mushroom-shaped structure at the top of the Pd-NWs. Fig. 1d shows the XRD patterns of MG NWs and Pt@MG NWs. Before Pt deposition, the MG NWs are fully glassy, characterized by a broad hump around 42°. For Pt@MG NWs, there exist several sharp diffraction peaks besides the amorphous peak. By checking powder diffraction file (PDF) cards, the Bragg diffraction peaks at 39°, 46° and 67° corresponded to the indices of the crystal face of Pt (111), (200), and (220), respectively. This was confirmed by the HAADF and selected area electron diffraction images obtained using a scanning transmission electron microscope with double spherical aberration correctors (Cs-STEM) shown in Fig. 1e, where Pt nanocrystals were embedded in the MG matrix. Fig. 1f–k show the element distribution, where Pt was abundant on the surface. The Pt@MG NW electrocatalyst was synthesized by depositing Pt on the surface of MG NWs.

Electrocatalytic performance of the catalyst

A standard two-compartment three-electrode system with a proton exchange membrane (PEM) was used to evaluate the electrocatalytic performance of the hybrid Pt@MG NW electrocatalyst for the HER in a 0.5 M H_2SO_4 electrolyte at room temperature. Fig. 2a shows the LSV curves of Pt@MG NWs, MG NWs, the polished MG plate and commercial Pt/C (10 wt% Pt) with current density normalized to the geometric area. All polarization curves were measured without IR compensation. Despite all four materials exhibiting catalytic activity for the HER, obvious differences in catalytic performance can be identified, where the overpotential required to achieve a geometric current density of 10 mA cm^{-2} is significantly different. The overpotential for MG NWs (113 mV) is much smaller than that for the MG plate (300 mV), demonstrating that the introduced nano structure is beneficial for increasing catalytic activity. Besides the increased surface areas after surface engineering, the small H_2 bubbles generated on the surface of the MG NWs can be rapidly released, while the active area of the MG plate electrode is decreased due to the adsorption of H_2 bubbles, which will be discussed later. The Pt@MG NW catalyst requires a much smaller overpotential of 48.5 mV, which is much lower than the 300 mV of the MG plate and 113 mV of MG NWs and close to that of commercial Pt/C (36 mV), suggesting an obvious improvement in the intrinsic catalysis of the HER due to Pt decoration. The Pt@MG NW catalyst exhibits higher catalytic activity compared to the commercial Pt/C catalysts when the overpotential is over 70 mV (as shown in ESI Fig. S3†). Pt@MG NWs also have HER catalytic activity comparable with Pt/C under alkaline conditions, as shown in Fig. S4.† The current density of Pt@MG NWs is higher than that of Pt/C under high overpotential.

To obtain further insight into the catalytic performance, the Tafel plots (overpotential η *vs.* logarithmic current density $\log(-j)$) of different catalysts are presented in Fig. 2b, where linear portions of the Tafel plots are fitted by the Tafel equation ($\eta = b \log j + a$, where j is the current density and b is the Tafel slope). The Tafel slope is an inherent property of a catalyst which is determined by the rate-limiting step in the HER. It is well-known that a small Tafel slope is advantageous for HER applications since it indicates a faster increase of the HER rate with increasing overpotential.[50] A Tafel slope of 36.8 mV dec^{-1} for commercial Pt/C can be observed, consistent with previous reports.[27,28,51,52] In addition, the Tafel slopes of the MG plate and MG NWs are 138.8 mV dec^{-1} and 90.7 mV dec^{-1}, respectively. That is to say, the large surface area provided by the nanowires significantly enhances the catalytic performance of the MG substrate. After decorating Pt particles on the nanowires, the Pt@MG NWs exhibit a remarkably low Tafel slope of 19.8 mV dec^{-1}, which is even smaller than that of the commercial Pt/C electrode and similar to that of Pt–Pd bimetallic nanoparticles on carbon catalysts.[53] The small Tafel slope of Pt@Pd-NWs suggests that the HER process follows a Volmer–Tafel mechanism.

As shown in Fig. 2c, electrochemical impedance spectroscopy (EIS) was employed to provide a further understanding of the catalytic performance. The EIS spectra of the MG plate, MG NWs, and Pt@MG NWs can be well fitted with a simple equivalent circuit, which consists of a constant phase element (CPE), series resistance (R_S), and charge-transfer resistance (R_{ct}). The MG plate, MG NWs and Pt@MG NWs have small series resistances (R_S). Meanwhile, the semicircular diameter in the EIS spectrum of the Pt@MG NW catalyst is considerably smaller than those of the MG plate and MG NWs due to its smaller charge-transfer resistance (R_{ct}), suggesting a faster reaction rate and higher charge transport efficiency. For Pt@MG NWs, the charge transfer resistance is closely related to the synergistic effects of the nanowire structure and the catalytic Pt active sites. By electroplating fine Pt particles onto the nanowires with good conductivity, more active sites are exposed on the surface, leading to lower charge-transfer resistance of the HER, which favors the catalytic activity under high overpotential. The electrochemically active surface area (ECSA) of the Pt@MG NWs was also estimated according to CV curves (shown in ESI Fig. S5 and S6†). A linear trend is observed for $\Delta J/2$ as a function of the scan rate, as shown in Fig. 2d. The slope represents geometric double-layer capacitance C_{dl}, which is linearly proportional to the ECSA; hence the ratio among the C_{dl} of different catalysts can be used to evaluate the ECSA. It is worth noting that the number of active sites on Pt@MG NWs was around 3 times higher than that on Pt/C, indicating that our synthesis strategy was beneficial for exposing more active sites for the catalytic

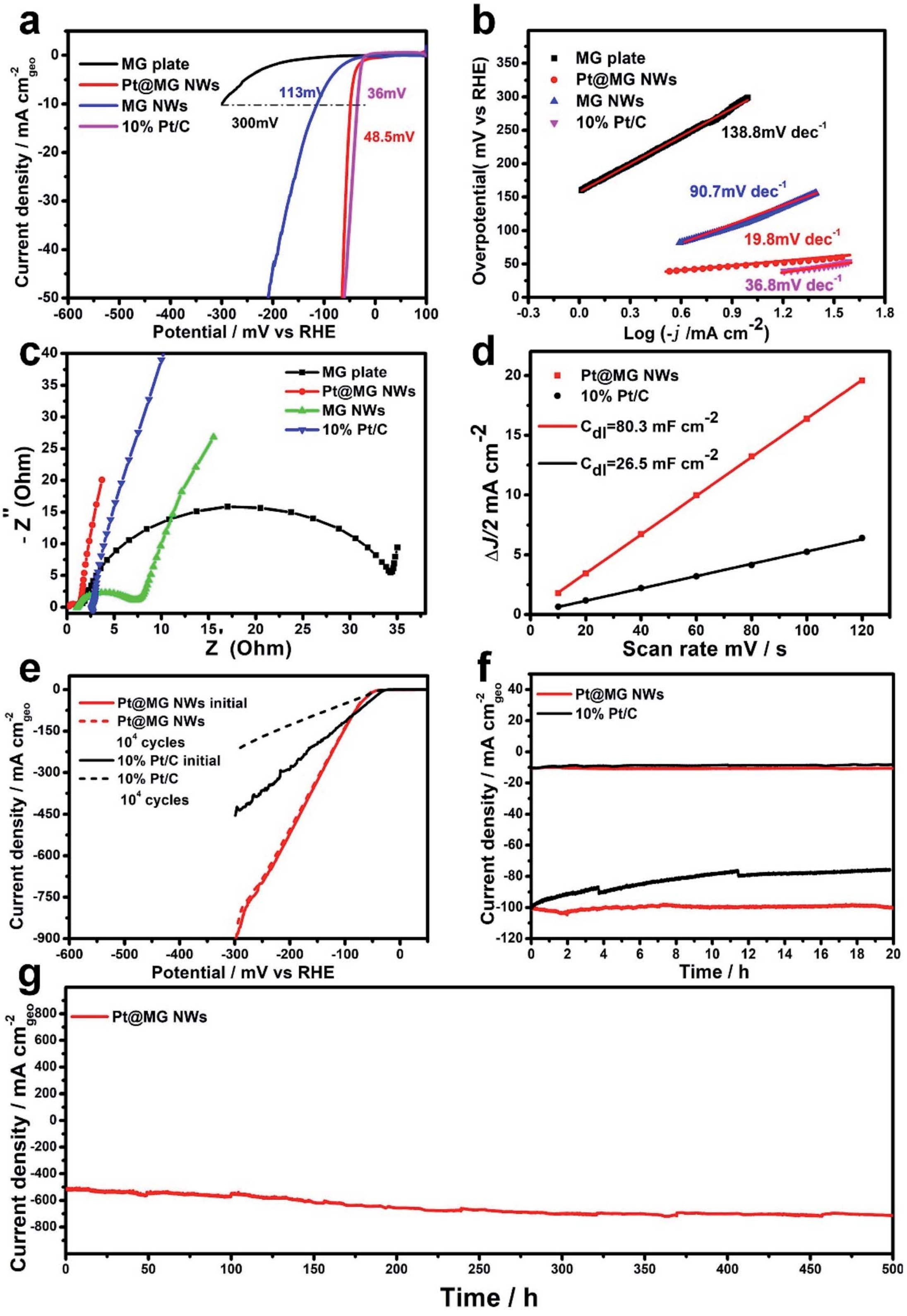

Fig. 2 Electrocatalytic property characterization. (a) The HER polarization curves for the MG plate, MG NWs, Pt@MG NWs and Pt/C catalysts acquired by linear sweep voltammetry with a scan rate of 2 mV s^{-1} in 0.5 M H_2SO_4 at room temperature. (b) Corresponding Tafel slope derived from (a) where the Tafel slope is identified. (c) EIS spectra of the MG plate and Pt@MG NWs at a 10 mV overpotential. (d) Plots of current densities against scan rates. Δj is the difference between the anodic and cathodic current density at a potential of 0.15 V *vs.* RHE. The slope of the fitted line is twice that of the electrochemical double-layer capacitance, which is proportional to the ECSA of the catalysts. (e) Polarization curves of Pt@MG NWs and Pt/C before and after 10 000 LSV cycles in 0.5 M H_2SO_4. (f) Stability tests of the Pt@MG NWs and Pt/C in 0.5 M H_2SO_4 under static overpotential to achieve current densities of 10 mA cm^{-2} and 100 mA cm^{-2}, respectively. (g) Stability test of the Pt@MG NW catalysts under a static overpotential of 200 mV in 0.5 M H_2SO_4.

reaction. To better reveal the difference in catalytic activity, the LSV curves of Pt@MG NWs and Pt/C were normalized by the mass of Pt and ECSA, respectively (as shown in Fig. S7†). At $\eta = 200$ mV, the mass current density of Pt@MG NWs reaches 136 445 A g^{-1} Pt, which is 3.35 times higher than that of Pt/C, and the current density normalized to the ECSA of Pt@MG NWs is 4.17 times higher than that of Pt/C, confirming the high catalytic activity of Pt@MG NWs.

In addition to activity, stability is another key concern for HER catalysts, especially for commercial usage. According to the polarization curves shown in Fig. 2e, the overpotential required to achieve a current density of 10 mA cm^{-2} for Pt/C increases from 36 mV to 50 mV after 10 000 cycles of the LSV test. In contrast, the value of Pt@MG NWs only increases from 48.5 mV to 50 mV, exhibiting negligible deterioration. Durability is another significant criterion to evaluate the performance of a HER catalyst, which was tested at different static overpotential levels in an acidic environment in the present work. Fig. 2f shows the time-dependent current density curves when different overpotentials for Pt@MG NWs (48.5 mV and 84 mV) and Pt/C (37 mV and 119 mV) were applied to achieve 10 mA cm^{-2} and 100 mA cm^{-2}, respectively. It can be seen that the current density of the Pt@MG NWs remains almost unchanged after the HER for 20 hours under both conditions. In sharp contrast, Pt/C shows obvious degradation under the same conditions. This behavior demonstrates that the activity of Pt/C decreases upon stability testing, while the activity of Pt@MG NWs is even more self-improved, which is consistent with previous reports.[45,46] More severe but significant conditions were also tested by applying a large overpotential of 200 mV. The time–current curve is presented in Fig. 2g; the non-monotonicity of the curve originated from the disruption in the applied potential. The driving current density could be as large as 600 mA cm^{-2} under this overpotential, which is significant for efficient evolution of hydrogen in the water electrolysis industry. At such a high overpotential, the small difference of the overpotential at 10 mA cm^{-2} between Pt@MG NWs and Pt/C is negligible owing to the low Tafel slope of Pt@MG NWs. Such excellent catalytic activity under large current originates from the high conductivity and high structural stability of the Pt nanoparticles embedded in the glassy matrix. As shown in Fig. S8,† the nanowire structure is stable after stability tests after 210 h, where no peeling off of nanowires is visible. The surface composition change of Pt@MG NWs before and after the stability test is characterized by using XPS. As shown in Fig. S9 and Table S4,† Ni and P entirely disappear from the surface, and an obvious decrease of the Cu content can be identified compared with the nominal composition, resulting in a surface abundant in Pt and Pd. The dealloying of the glassy matrix upon electrochemical testing exposes more active sites, leading to self-enhanced catalytic performance under long-term testing.

Nano structure enhanced HER

The surface structure of the catalysts could improve the HER properties.[54–56] To illustrate the structural origin of the high catalytic activity of Pt@MG NWs, contact angle tests of the MG plate and MG NWs were performed. As shown in Fig. 3a and c, the contact angles of water drops and bubbles were 87 ± 3° and 117 ± 2°, respectively, on the smooth surface of the MG plate. In contrast, as shown in Fig. 3b and d, the contact angles of water drops and bubbles were 24 ± 1° and 132 ± 1° on the surface of MG NWs. Fig. 3e and f show the dynamic contact performance of MG NWs. The droplet contact angle quickly changed from 58° to 27° in a short time of less than 2 seconds, showing superb hydrophilicity. The bubble contact angle on MG NWs is almost unchanged and stabilized at 132 ± 1°. Fig. 3g summarizes the dynamic water and bubble contact performance for MG NWs and the MG plate. The excellent hydrophilicity and aerophobicity of the MG NW surface played an important role in the HER process.[57,58] As shown in Fig. 3h, due to the hydrophilicity of the MG NW surface, the surface of MG NWs had a larger contact surface area with the electrolyte compared with the smooth and unstructured surface of the MG plate at the same size, which made the water molecules in the electrolyte easier to bring into contact with the active sites, thus greatly improving the reaction rate. When water molecules in the solution reacted to produce hydrogen bubbles on the surface, the excellent aerophobicity of the MG NW surface made the small bubbles escape from the surface easily, which could ensure that the generated bubbles would not occupy the active sites. Therefore, the hydrophilic and aerophobic MG NWs provide easier channels for water molecules to react on active sites and for bubbles to escape compared with the unstructured substrate, making it an efficient catalyst supporter for the HER.

The adsorption energy and Gibbs free energy of Pt@MG NWs based on first principles calculation

To further investigate the mechanism, density functional theory (DFT) calculations were carried out. Considering the continuous surface composition change resulting from dealloying during electrochemical tests, in this study, four computational models were considered, including Pd_{64}, Pt_{64}, $Pd_{48}Pt_{16}$ and $Pd_{16}Pt_{48}$, covering a large composition range. First of all, the H* adsorption strength (ΔE_{H^*}) of HER intermediates on the catalyst can reflect the adsorption ability. Taking $Pd_{48}Pt_{16}$ as an example, the adsorption model of H* on the catalyst was constructed as shown in Fig. 4a and b. According to the calculated ΔE_{H^*} results of the different models (Fig. 4c), the Pt site always has the strongest adsorption capacity compared with the Pd site. The pure Pt (Pt_{64}) exhibits the strongest adsorption energy (−0.623 eV); the $Pd_{48}Pt_{16}$–Pt (−0.529 eV) and $Pd_{16}Pt_{48}$–Pt (−0.619 eV) also show strong adsorption capacity. In contrast, the adsorption energies of the Pd site are positive (>0), indicating that the Pd site is not conducive to the adsorption of H atoms.

An optimal HER activity can be achieved at a value of ΔG_{H^*} close to zero ($\Delta G_{H^*} \sim 0$), indicating that HER reaction is easily spontaneous. Lower ΔG_{H^*} will result in strong bonding of adsorbed H, while higher ΔG_{H^*} will lead to the protons bonded too weakly, both leading to slow HER process. The calculated ΔG_{H^*} of different models are shown in Fig. 4d. Although the

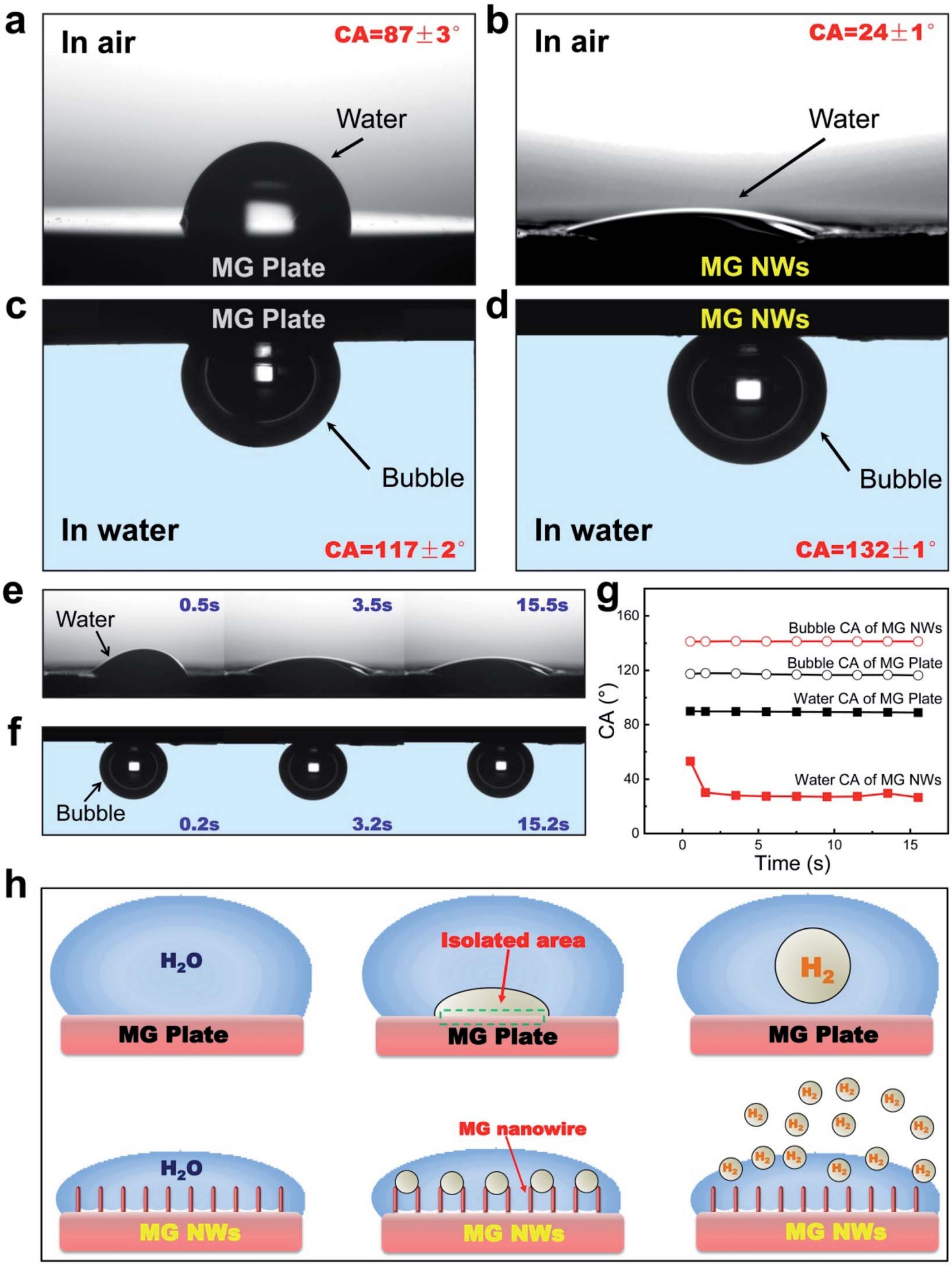

Fig. 3 The excellent hydrophilicity and aerophobicity of the nano engineered surface. (a) Contact angle of the MG plate with a water droplet; (b) contact angle of MG NWs with a water droplet; (c) contact angle of the MG plate with a bubble; (d) contact angle of MG NWs with a bubble; (e) the evolution of a water drop on MG NWs at the initial stage; (f) the evolution of a bubble on MG NWs at the initial stage; (g) evolution of contact angle *versus* time under different test conditions; (h) sketch of the HER on the surface of the MG plate and MG NWs.

ΔE_{H^*} of $Pd_{48}Pt_{16}$–Pt is weak than the Pt_{64} and $Pd_{16}Pt_{48}$–Pt, $Pd_{48}Pt_{16}$–Pt exhibits the smallest $|\Delta G_{H^*}|$ value of 0.217 eV. The $|\Delta G_{H^*}|$ of $Pd_{48}Pt_{16}$–Pt is lower than that of the optimal Pd_{64} (0.435 eV), $Pd_{48}Pt_{16}$–Pd (0.406 eV), $Pd_{16}Pt_{48}$–Pd (0.471 eV), Pt_{64} (0.311 eV) and $Pd_{16}Pt_{48}$–Pt (0.307 eV), indicating that the $Pd_{16}Pt_{48}$ (a small amount Pt mixed) surface possesses superior HER activity than pure Pd or Pt (see ESI Fig. S10 and Table S1†). The above calculated results demonstrate that alloying smaller Pt into Pd can affect the electronic charge redistribution of the catalyst surface. To further illustrate the electronic charge redistribution, the projected density of states (PDOS) of the selected H, Pd and Pt site was calculated and shown in ESI

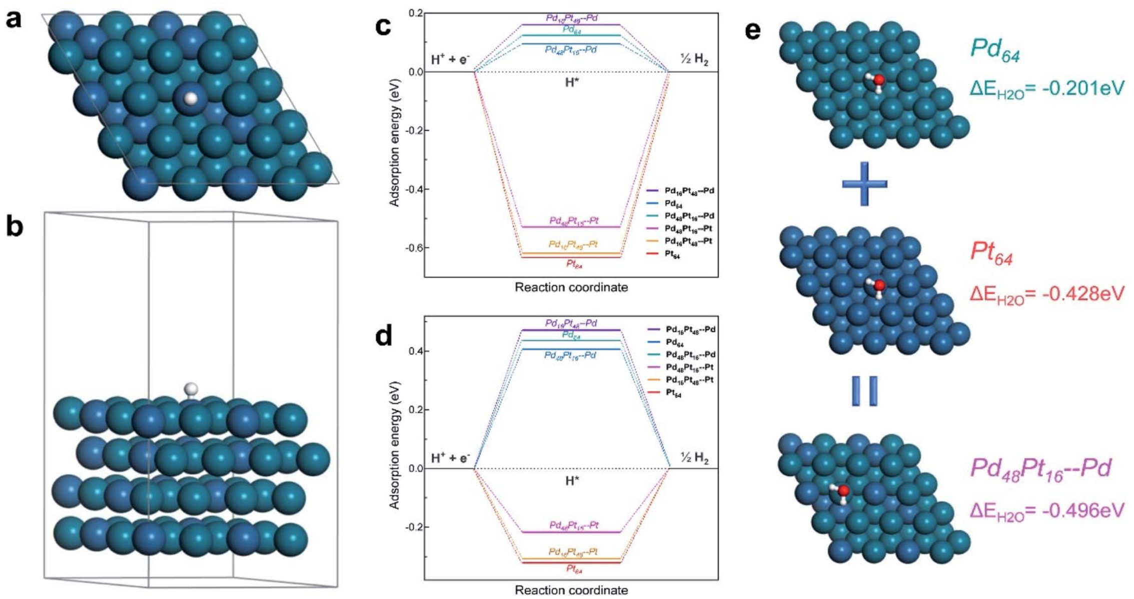

Fig. 4 Density functional theory (DFT) calculations. (a) Top view and (b) 3D view of the $Pd_{48}Pt_{16}$–Pt atomic configuration. (c) Calculated H* absorption energy and (d) Gibbs free energy changes on Pd_{64}, $Pd_{48}Pt_{16}$–Pd, $Pd_{16}Pt_{48}$–Pd, Pt_{64}, $Pd_{48}Pt_{16}$–Pt and $Pd_{16}Pt_{48}$–Pt models. (e) H_2O adsorption energies for the Pd_{64}, Pt_{64}, and $Pd_{48}Pt_{16}$–Pt models.

Fig. S11.† Therefore, the H* adsorption of the catalyst becomes easier, resulting in an enhanced HER activity of the hybrid catalyst.

Additionally, the H_2O^* adsorption energies of different models are also calculated as shown in Fig. 4d (see Fig. S12 and Tables S2 in the ESI†). According to the calculated results, the hybrid ($Pd_{48}Pt_{16}$–Pt) exhibits stronger H_2O adsorption energy ($\Delta E_{H_2O^*} = -0.521$ eV) than Pd_{64} (−0.201 eV) and Pt_{64} (−0.428 eV), indicating a more considerable collection of H_2O (initial reactant state) on the surface of the hybrid $Pd_{48}Pt_{16}$. This further implies that the Pt mixed hybrid catalyst accelerates the process of the HER.

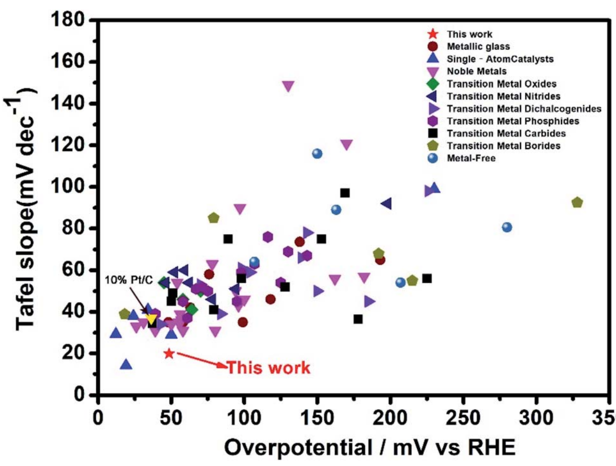

Fig. 5 Overpotential and Tafel slope comparisons of the HER catalyst in the present work with different categories reported in previous literature. More details can be found in ESI Table S5.†

The Tafel slope and overpotential @ 10 mA cm^{-2} of our catalysts were compared with those of HER electrocatalysts reported in the literature including single-atom catalysts, noble metals, transition metal oxides, transition metal nitrides, transition metal dichalcogenides, transition metal phosphides, transition metal carbides, transition metal borides, metallic glasses and metal-free catalysts (see Fig. 5 and ESI Table S5†). It is encouraging to see that the performance of the hybrid Pt@MG NW catalyst is superior to that of most previously reported catalysts for the HER in acidic solution. Both a low overpotential and Tafel slope can be obtained with this catalyst. This work proposes a flexible and universal strategy to synthesise MG based hybrid catalysts. The hydrophilic and aerophobic nanowire structure with large specific area could significantly increase the activity. The stable structure of Pt nanoparticles embedded in the glassy matrix ensures long-term stability with large current density. The dealloying of the glassy matrix leads to self-enhanced catalytic activity upon long-term usage.

Conclusions

In summary, we have developed a flexible and universal strategy to fabricate an efficient and robust catalyst for the HER. Through thermoplastic forming, the surface of MG can be engineered into desired structures down to the nano scale acting as a supporter of the catalyst. By decorating Pt particles on the nanowires, the electrocatalyst Pt@MG NWs show superior performance for the HER with an overpotential of 48.5 mV @ 10 mA cm^{-2} under acidic conditions. Astonishingly, the Tafel slope is only 19.8 mV dec^{-1}, smaller than that of 10% Pt/C. The EIS measurement shows that the Pt@MG NW catalyst has excellent charge transport efficiency. The ECSA results show that the number of active sites in Pt@MG NWs was around 3 times higher than that in Pt/C. In addition, the Pt@MG NW catalyst is ultra-stable exhibiting no degradation after the HER under overpotentials of 48.5 mV and 84 mV for 20 hours and under an extremely high overpotential of 200 mV for 500 hours. The hydrophilicity and aerophobicity of Pt@MG NWs are responsible for the outstanding HER performance and originate from the surface structural construction. Our results provide a novel and universal approach for designing superior HER catalysts with excellent activity and stability.

Author contributions

J. M. and J. S. supervised the work. Y. Y. and C. W. designed and conducted the electrochemical experiments. Z. H. and J. F. carried out the scanning electron microscope and transmission electron microscope observations and performed the metallic glass ribbon preparation, calorimetry and X-ray diffraction tests. Z. X. and L. Z. conducted the simulations. J. M., Y. Y. and C. W. wrote the manuscript. All the authors contributed to the analysis and interpretation of the data and to the development and editing of the manuscript.

Conflicts of interest

The authors declare no competing financial interest.

Acknowledgements

This work was supported by the Science and Technology Innovation Commission Shenzhen (Grants No. JCYJ20170412111216258), the Natural Science Foundation of Guangdong Province (Grant No. 2019B030302010), the National Science Foundation of China (Grant No. 51871157 and 51801095), and the National Key Research and Development Program of China (Grant No. 2018YFA0703605). The authors are grateful for the help on the microscope observation received from the Electron Microscope Center of Shenzhen University.

References

1 J. Zhang and X. Wang, *Angew. Chem.*, 2015, **54**, 7230–7232.

2 Y. Yan, B. Y. Xia, B. Zhao and X. Wang, *J. Mater. Chem.*, 2016, **4**, 17587–17603.

3 Y. Li, H. Wang, L. Xie, Y. Liang, G. Hong and H. Dai, *J. Am. Chem. Soc.*, 2011, **133**, 7296–7299.

4 E. J. Popczun, J. R. Mckone, C. G. Read, A. J. Biacchi, A. M. Wiltrout, N. S. Lewis and R. E. Schaak, *J. Am. Chem. Soc.*, 2013, **135**, 9267–9270.

5 J. A. Turner, *Science*, 2004, **305**, 972–974.

6 J. Greeley, T. F. Jaramillo, J. Bonde, I. Chorkendorff and J. K. Norskov, *Nat. Mater.*, 2006, **5**, 909–913.

7 D. Merki and X. Hu, *Energy Environ. Sci.*, 2011, **4**, 3878–3888.

8 Y. Jiao, Y. Zheng, M. Jaroniec and S. Qiao, *Chem. Soc. Rev.*, 2015, **44**, 2060–2086.

9 I. A. Raj and K. I. Vasu, *J. Appl. Electrochem.*, 1990, **20**, 32–38.

10 A. Döner, R. Solmaz and G. Kardaş, *Int. J. Hydrogen Energy*, 2011, **36**, 7391–7397.

11 R. Solmaz and G. Kardaş, *Electrochim. Acta*, 2009, **54**, 3726–3734.

12 B. Hinnemann, P. G. Moses, J. Bonde, K. P. Jorgensen, J. H. Nielsen, S. Horch, I. Chorkendorff and J. K. Norskov, *J. Am. Chem. Soc.*, 2005, **127**, 5308–5309.

13 H. Wang, Z. Lu, S. Xu, D. Kong, J. J. Cha, G. Zheng, P. Hsu, K. Yan, D. Bradshaw and F. B. Prinz, *Proc. Natl. Acad. Sci. U. S. A.*, 2013, **110**, 19701–19706.

14 J. Xie, H. Zhang, S. Li, R. Wang, X. Sun, M. Zhou, J. Zhou, X. W. D. Lou and Y. Xie, *Adv. Mater.*, 2013, **25**, 5807–5813.

15 D. Voiry, M. Salehi, R. Silva, T. Fujita, M. Chen, T. Asefa, V. B. Shenoy, G. Eda and M. Chhowalla, *Nano Lett.*, 2013, **13**, 6222–6227.

16 D. Kong, H. Wang, J. J. Cha, M. Pasta, K. J. Koski, J. Yao and Y. Cui, *Nano Lett.*, 2013, **13**, 1341–1347.

17 A. B. Laursen, S. Kegnaes, S. Dahl and I. Chorkendorff, *Energy Environ. Sci.*, 2012, **5**, 5577–5591.

18 H. Wang, D. Kong, P. Johanes, J. J. Cha, G. Zheng, K. Yan, N. Liu and Y. Cui, *Nano Lett.*, 2013, **13**, 3426–3433.

19 W. Chen, C. H. Wang, K. Sasaki, N. Marinkovic, W. Xu, J. T. Muckerman, Y. Zhu and R. R. Adzic, *Energy Environ. Sci.*, 2013, **6**, 943–951.

20 H. Vrubel and X. Hu, *Angew. Chem.*, 2012, **51**, 12703–12706.

21 H. I. Karunadasa, E. Montalvo, Y. Sun, M. Majda, J. R. Long and C. J. Chang, *Science*, 2012, **335**, 698–702.

22 W. Chen, K. Sasaki, C. Ma, A. I. Frenkel, N. Marinkovic, J. T. Muckerman, Y. Zhu and R. R. Adzic, *Angew. Chem.*, 2012, **51**, 6131–6135.

23 B. Cao, G. M. Veith, J. C. Neuefeind, R. R. Adzic and P. G. Khalifah, *J. Am. Chem. Soc.*, 2013, **135**, 19186–19192.

24 Q. Liu, J. Tian, W. Cui, P. Jiang, N. Cheng, A. M. Asiri and X. Sun, *Angew. Chem.*, 2014, **53**, 6710–6714.

25 M. Zhou, Q. Sun, Y. Shen, Y. Ma, Z. Wang and C. Zhao, *Electrochim. Acta*, 2019, **306**, 651–659.

26 D. Kong, H. Wang, Z. Lu and Y. Cui, *J. Am. Chem. Soc.*, 2014, **136**, 4897–4900.

27 S. A. Grigoriev, P. Millet and V. N. Fateev, *J. Power Sources*, 2008, **177**, 281–285.

28 B. Ruqia and S. Choi, *ChemSusChem*, 2018, **11**, 2643–2653.

29 J. Yuan, Y. Liu, T. Bo and W. Zhou, *Int. J. Hydrogen Energy*, 2020, **45**, 2681–2688.

30 K. M. Naik, E. Higuchi and H. Inoue, *Nanoscale*, 2020, **12**, 11055–11062.

31 X. Zhao, Z. Yang, W. Wang, Y. Li, X. Zhou and H. Zhang, *J. Mater. Chem. A*, 2020, **8**, 7171–7176.

32 D. Li, X. Chen, Y. Lv, G. Zhang, Y. Huang, W. Liu, Y. Li, R. Chen, C. Nuckolls and H. Ni, *Appl. Catal., B*, 2020, **269**, 118824.

33 L. Zhang, K. Doyledavis and X. Sun, *Energy Environ. Sci.*, 2019, **12**, 492–517.

34 M. Wu, P. K. Shen, Z. Wei, S. Song and M. Nie, *J. Power Sources*, 2007, **166**, 310–316.

35 D. Fang, L. Wan, Q. Jiang, H. Zhang, X. Tang, X. Qin, Z. Shao and Z. Wei, *Nano Res.*, 2019, **12**, 2766–2773.

36 K. Jiang, D. Zhao, S. Guo, X. Zhang, X. Zhu, J. Guo, G. Lu and X. Huang, *Sci. Adv.*, 2017, **3**, e1601705.
37 C. A. Schuh, T. C. Hufnagel and U. Ramamurty, *Acta Mater.*, 2007, **55**, 4067–4109.
38 W. L. Johnson, *MRS Bull.*, 1999, **24**, 42–56.
39 M. Telford, *Mater. Today*, 2004, **7**, 36–43.
40 A. Peker and W. L. Johnson, *Appl. Phys. Lett.*, 1993, **63**, 2342–2344.
41 Z. P. Lu and C. T. Liu, *Acta Mater.*, 2002, **50**, 3501–3512.
42 W. Klement, R. H. Willens and P. Duwez, *Nature*, 1960, **187**, 869–870.
43 A. Inoue, *Acta Mater.*, 2000, **48**, 279–306.
44 J. Ma, Z. Huang, H. Zheng, F. Gong and X. Liang, *Mater. Res. Express*, 2019, **6**, 075210.
45 Y. C. Hu, Y. Z. Wang, R. Su, C. R. Cao, F. Li, C. W. Sun, Y. Yang, P. F. Guan, D. W. Ding and Z. L. Wang, *Adv. Mater.*, 2016, **28**, 10293–10297.
46 F. Hu, S. Zhu, S. Chen, Y. Li, L. Ma, T. Wu, Y. Zhang, C. Wang, C. Liu, X. Yang, L. Song, X. Yang and Y. Xiong, *Adv. Mater.*, 2017, **29**, 1606570.
47 S. Bai, D. C. Wang, D. M. Deng, P. M. Gong, Y. Bai, P. J. Jiang and P. Y. Xiong, *Angew. Chem., Int. Ed.*, 2014, **53**, 12120–12124.
48 A. Navaee and A. Salimi, *Electrochim. Acta*, 2016, **211**, 322–330.
49 T. Wu, G. Wang, Y. Zhang, S. Kang and H. Zhang, *New J. Chem.*, 2017, **41**, 7012–7019.
50 B. E. Conway and L. Bai, *J. Electroanal. Chem.*, 1986, **198**, 149–175.
51 J.-S. Moon, J.-H. Jang, E.-G. Kim, Y.-H. Chung, S. J. Yoo and Y.-K. Lee, *J. Catal.*, 2015, **326**, 92–99.
52 E. J. Popczun, C. G. Read, C. W. Roske, N. S. Lewis and R. E. Schaak, *Angew. Chem., Int. Ed.*, 2014, **53**, 5427–5430.
53 S. Bai, C. Wang, M. Deng, M. Gong, Y. Bai, J. Jiang and Y. Xiong, *Angew. Chem., Int. Ed.*, 2014, **53**, 12120–12124.
54 Y. Li, H. Wang, L. Xie, Y. Liang, G. Hong and H. Dai, *J. Am. Chem. Soc.*, 2011, **133**, 7296–7299.
55 Y. C. Dong, S. K. Park, Y. H. Chung, S. H. Yu, D. H. Lim, N. Jung, H. C. Ham, H. Y. Park, Y. Piao and S. J. Yoo, *Nanoscale*, 2014, **6**, 10584–10588.
56 K. Wu, *Acta Phys.-Chim. Sin.*, 2017, **33**, 1027–1032.
57 X. Zhao, H. Ren and L. Luo, *Langmuir*, 2019, **35**, 5392–5408.
58 S. Niu, W. Jiang, T. Tang, L. Yuan, H. Luo and J. Hu, *Adv. Funct. Mater.*, 2019, **29**, 1902180.